ROYAL SOCIETY
OF CHEMISTRY

Check for updates

A facile self-saturation process enabling the stable cycling of a small molecule menaquinone cathode in aqueous zinc batteries†

Shuo Li,[a] Guoli Zhang,*[a] Qianrui Li,[a] Tianshun He[a] and Xiaoqi Sun ⓘ *[ab]

Small quinone molecules are promising cathode materials for aqueous zinc batteries. However, they experience fast capacity decay due to dissolution in electrolytes. Herein, we introduce a simple methyl group to a naphthoquinone (NQ) cathode and demonstrate a facile self-saturation strategy. The methyl group exhibits hydrophobic properties together with light weight and a weak electron-donation effect, which allows a good balance among cycling stability, capacity and voltage for cathode materials. The resulting menadione (Me-NQ) presents around one-third solubility of NQ. The former thus rapidly reaches saturation in the electrolyte during cycling, which suppresses subsequent dissolution. Thanks to this process, the Me-NQ cathode preserves 146 mA h g^{-1} capacity after 3500 cycles at 5 A g^{-1}, far exceeding 88 mA h g^{-1} for NQ. Me-NQ also delivers a stabilized capacity of 316 mA h g^{-1} at 0.1 A g^{-1} with only 0.05 V lower average redox voltage than NQ. The co-storage of Zn^{2+} and H$^+$ with the redox reactions on the carbonyl sites of Me-NQ is revealed.

Introduction

Rechargeable aqueous batteries are attracting great attention for large-scale energy storage systems owing to their advantages of high safety, low cost and environmental friendliness.[1–12] The Zn metal is one of the most desired anode candidates with high theoretical specific capacity (820 mA h g^{-1}; 5855 mA h cm^{-3}), low redox potential (−0.76 V *vs.* S.H.E.) and high stripping/plating reversibility in aqueous electrolytes.[8,13–18] The design and optimization of cathode materials play an important role in battery performance. Current research on cathode materials mainly focuses on inorganic compounds such as metal oxides,[10,20,21] polyanion compounds,[22–27] elements,[28–31] and organic materials.[6,8,12,14,17,19] Among them, organic compounds provide high flexibility of molecular structure designs, which allow the control of electrochemical properties. A variety of functional groups on organic materials have been revealed to show feasible redox activities in batteries, such as carbonyl,[32] imine,[33] and azo.[34]

Among organic cathode candidates, small molecule quinones with carbonyl groups as active sites present the ease of synthesis, high capacity and high reaction reversibility. For example, Kundu *et al.* proposed a *p*-chloranil cathode in aqueous zinc batteries, delivering a specific capacity of 205 mA h g^{-1} at 0.2C.[32] Zhang *et al.* uncovered the effect of hydrogen bonding for cation storage capability of quinone-based small molecules and achieved a specific capacity of 180.3 mA h g^{-1} at 5 A g^{-1} with an ultra-high loading of 66.2 mg cm^{-2} for a 2,5-diaminocyclohexa-2,5-diene-1,4-dione (DABQ) cathode.[35] Our group revealed facile proton transport through the Grotthuss-type mechanism in tetraamino-*p*-benzoquinone (TABQ), which reached 308 mA h g^{-1} capacity at 0.1 A g^{-1} and retained 213 mA h g^{-1} at 5 A g^{-1}.[36] We also showed that the substitution sites of methoxy groups on quinone affected the charge distribution and furthermore their electrochemical performance.[37] Despite the promising electrochemical activity of small molecule quinones in aqueous zinc cells, they exhibit relatively high solubility in electrolytes. It results in the facile loss of active material from the cathode and thus fast capacity decay especially at lower current densities. Current solutions to the dissolution problem include polymerization,[38,39] compositing with other materials,[40] introducing hydrophobic sites,[14] *etc.* Among them, molecular structure regulation would fundamentally solve the related issues. Nevertheless, the possible introduction of dead weight and influence on the redox potential of carbonyl sites should also be taken into consideration for the electrochemical performance of designed cathode molecules.

Balancing the overall requirements of high cycling stability, capacity and redox potential for cathode materials, the hydrophobic methyl group with relatively light weight and a weak electron-donation effect is a desired substitution candidate. Herein, we introduce a methyl group on the 1,4-

[a]Department of Chemistry, Northeastern University, Shenyang 110819, China. E-mail: 2210076@stu.neu.edu.cn; sunxiaoqi@mail.neu.edu.cn

[b]National Frontiers Science Center for Industrial Intelligence and Systems Optimization, Northeastern University, 3-11 Wenhua Road, Shenyang, 110819, China

† Electronic supplementary information (ESI) available. See DOI: https://doi.org/10.1039/d4sc04685d

naphthoquinone (NQ) molecule to form a menaquinone (Me-NQ) cathode for aqueous zinc cells. As expected, the solubility of Me-NQ is effectively reduced to around one-third of NQ, together with only 8% reduction in theoretical capacity and a 0.05 V decrease in average redox voltage. In zinc cells, the low solubility of Me-NQ ensures its facile self-saturation in the electrolyte, as confirmed by *in situ* UV-vis analysis, which suppresses further active material dissolution from the cathode. Therefore, the capacity of Me-NQ stabilizes at 316 mA h g^{-1} at 0.1 A g^{-1}, and a good capacity of 146 mA h g^{-1} is retained after 3500 cycles at 5 A g^{-1}. For NQ, in contrast, the dissolution continues and capacity rapidly drops to 203 mA h g^{-1} after only 5 cycles at 0.1 A g^{-1} and 88 mA h g^{-1} after 3500 cycles at 5 A g^{-1}. Further studies confirm the facilitated reaction kinetics with the Me-NQ cathode and the redox reactions on carbonyl sites together with the co-storage of Zn^{2+} and protons.

Results and discussion

Fig. 1a shows the molecular structures of Me-NQ and NQ. Their morphologies are presented in the scanning electron microscopy (SEM) image in Fig. S1,† and the structures are confirmed by nuclear magnetic resonance (NMR, Fig. S2†). Thanks to the light weight of the methyl group, the theoretical capacity of Me-NQ is only slightly reduced to 311 mA h g^{-1} in comparison to 339 mA h g^{-1} for NQ. The frontier molecular orbital energy levels of the two molecules are calculated (Fig. 1b). It results in the lowest unoccupied molecular orbital (LUMO) levels of −3.10 eV and −3.19 eV for Me-NQ and NQ, respectively. The small difference is attributed to the weak electron-donation properties of the methyl group.[41] It indicates a minimal decrease of redox potential for Me-NQ, which is correlated with

the LUMO levels.[33,42] The solubilities of Me-NQ and NQ in the 2 M ZnSO$_4$ electrolyte are measured by ultraviolet-visible (UV-Vis) spectroscopy (Fig. 1c and d). Importantly, Me-NQ exhibits a low solubility of 0.186 mM, which is only around one third of 0.513 mM for NQ. It results from the introduction of the hydrophobic methyl group on the former and would further ensure enhanced cycling stability in zinc cells.

The electrochemical performance of the NQ and Me-NQ cathode materials is studied in aqueous zinc cells. Fig. 2a–c show the capacity and charge–discharge curves at different current densities. Notably, the capacity of the NQ cathode decays rapidly over cycling. It only retains 203 mA h g^{-1} capacity after 5 cycles at 0.1 A g^{-1}, which further decreases to 175 mA h g^{-1}, 128 mA h g^{-1}, 106 mA h g^{-1}, 93 mA h g^{-1}, 88 mA h g^{-1}, and 85 mA h g^{-1} with the increase of current density to 0.2 A g^{-1}, 0.5 A g^{-1}, 1 A g^{-1}, 2 A g^{-1}, 3 A g^{-1} and 5 A g^{-1}, respectively. A low capacity of 175 mA h g^{-1} is obtained when the current density returns to 0.1 A g^{-1}. With the Me-NQ cathode, in contrast, the capacity stabilizes fast within the initial couple cycles and reaches 316 mA h g^{-1} after 5 cycles at 0.1 A g^{-1}. It also shows stable evolution at the same current densities during the subsequent rate tests and delivers 287 mA h g^{-1}, 248 mA h g^{-1}, 233 mA h g^{-1}, 224 mA h g^{-1}, 218 mA h g^{-1} and 213 mA h g^{-1} at 0.2 A g^{-1}, 0.5 A g^{-1}, 1 A g^{-1}, 2 A g^{-1}, 3 A g^{-1} and 5 A g^{-1}, respectively. When the current density returns to 0.1 A g^{-1}, the capacity retrieves to 304 mA h g^{-1}. The self-discharge behaviors of the two cathodes are measured by resting the cells at the charged state for 48 h (Fig. 2d and e). The NQ cathode only preserves 75.3% capacity after the rest period, and it largely increases to 97.3% with the introduction of the methyl group. Meanwhile, thanks to the weak electron-donation effect of the methyl group, the Me-NQ cathode only exhibits slightly reduced average redox voltage at 0.83 V in comparison to 0.88 V for NQ (Fig. S3†). As a result, the energy densities of the Me-NQ cathode largely exceed those for NQ as compared in the Ragone plots in Fig. 2f.

The long-term cycling performance of the two cathodes is studied (Fig. 2g and S4†). The NQ cathode exhibits rapid capacity decays especially during the early stages of cycling. As a result, it only retains 153 mA h g^{-1} capacity after 100 cycles at a low current density of 0.2 A g^{-1} and 88 mA h g^{-1} after 3500 cycles at a high current density of 5 A g^{-1}. In contrast, much more stable cycling performance is obtained with the Me-NQ cathode. It preserves a good capacity of 236 mA h g^{-1} after 100 cycles at 0.2 A g^{-1} and 146 mA h g^{-1} after 3500 cycles at 5 A g^{-1}. This performance is comparable with that of previously reported organic cathode materials (Table S1†). Importantly, the Fourier-transform infrared (FT-IR) spectrum and SEM image of the Me-NQ cathode after long-term cycling suggest the preservation of characteristic vibration peaks and morphology (Fig. S5†). This confirms its excellent structural and morphological stability during electrochemical processes.

The above electrochemical tests demonstrate the superior cycling stability of the Me-NQ cathode in comparison to NQ. In order to reveal the underlying mechanism, *in situ* UV-vis spectroscopy is carried out for the electrolytes with Me-NQ and NQ cathodes, respectively. As shown in Fig. 3a, an absorption band
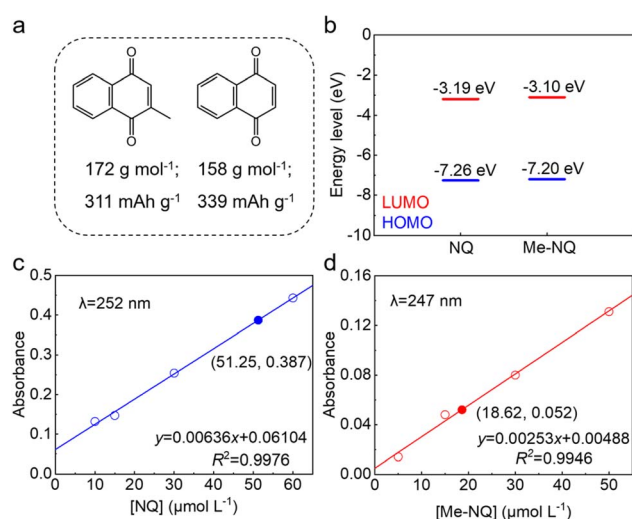

Fig. 1 (a) Molecular structures of Me-NQ (left) and NQ (right). (b) Calculated frontier molecular orbital energy levels of Me-NQ and NQ. UV-vis analysis to calculate the solubilities in 2 M ZnSO$_4$: the calibration curves and absorbance of 10 times diluents of saturated (c) NQ and (d) Me-NQ.
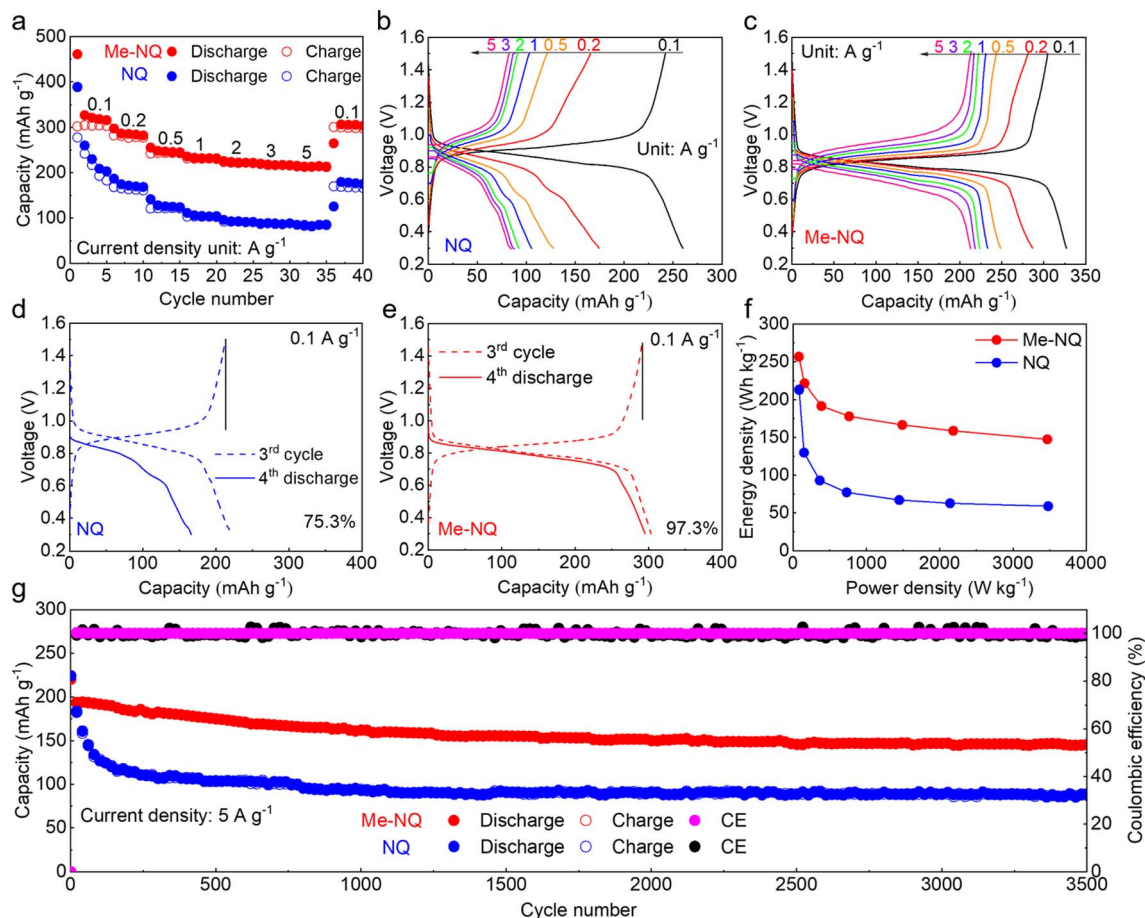
Fig. 2 (a) Rate performance of Me-NQ and NQ. Charge–discharge curves at different current densities of (b) NQ and (c) Me-NQ. Self-discharge tests of (d) NQ and (e) Me-NQ (resting at the charged state for 48 h). (f) Ragone plots (based on active material mass loading) of Me-NQ and NQ. (g) Cycling performance of Me-NQ and NQ at a current density of 5 A g^{-1}.

is noted at around 250 nm at the beginning of the discharge process of the NQ cathode. It keeps increasing together with the appearance and growth of another band at 330 nm upon the subsequent discharge and charge. They are attributed to the continuously dissolved active material from the cathode. Interestingly, the spectra of the electrolyte with the Me-NQ cathode show similar evolutions of absorption bands, though with much weaker peak intensities (Fig. 3b). This suggests that the Me-NQ active material also experiences dissolution at the beginning of cycling in zinc cells; nevertheless, the process is effectively suppressed thanks to its much lower solubility than NQ. *In situ* UV-vis analysis is further carried out for the two electrolytes with the cathodes cycled for 4 cycles. As shown in Fig. 3c, the peak intensity with the NQ cathode keeps increasing upon cycling and reaches the highest absorbance of 1.3 after 4 cycles. This suggests the severe and continuous dissolution of the active material, which results in fast capacity decay. In the electrolyte with the Me-NQ cathode, in contrast, the peak intensity quickly reaches a maximum absorbance of 0.33 after only two cycles and remains stable (Fig. 3d). This corresponds to the facile saturation of the active material in the electrolyte and equilibrium of the dissolution process. This self-saturation

behavior inhibits the subsequent continuous dissolution. Therefore, the majority of the active material stays on the cathode and delivers electrochemical activity, ensuring the stabilization of capacity in zinc cells.

To further demonstrate this self-saturation behavior, the active material loading is increased to 4 mg cm^{-2}, which reduces the percentage of dissolved parts with respect to the total material. The cycling test is carried out at 0.2 A g^{-1}. As shown in Fig. 3e and f, the NQ cathode still experiences facile capacity decay within the first 10 cycles and retains only 79 mA h g^{-1} capacity after 100 cycles. For the Me-NQ cathode, in contrast, a much more stable capacity retention is realized. It preserves a much higher capacity of 258 mA h g^{-1} after 100 cycles together with excellent preservation of charge–discharge curve shapes. This is also higher than 236 mA h g^{-1} with about 1.1 mg cm^{-2} active material loading, confirming the self-saturation mechanism.

The reaction kinetics of the two cathode materials in zinc cells are further studied. Electrochemical impedance spectroscopy (EIS) is carried out, and the Nyquist plots are fitted with the typical equivalent circuit shown in the inset (Fig. 4a). This results in a charge transfer resistance (R_{ct}) of 317 Ω for NQ,
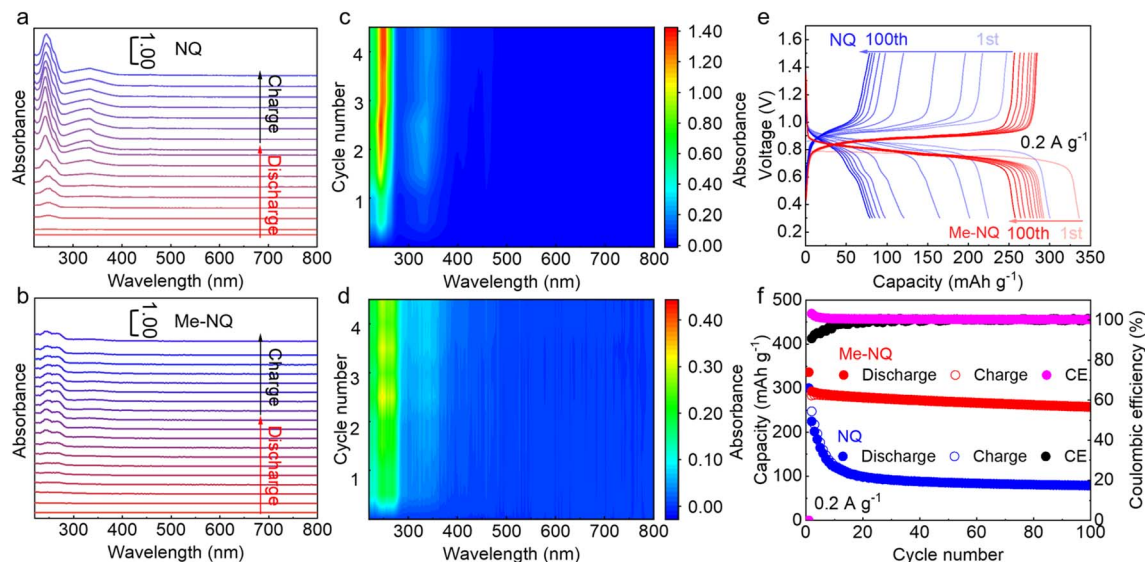
Fig. 3 *In situ* UV-vis spectra of the first cycle of the 2 M $ZnSO_4$ electrolyte with (a) NQ and (b) Me-NQ cathodes at 0.2 A g^{-1}. *In situ* UV-vis spectra of the 2 M $ZnSO_4$ electrolyte with (c) NQ and (d) Me-NQ cathodes at 0.5 A g^{-1}. (e) Charge/discharge curves at different cycles and (f) capacity evolutions of Me-NQ and NQ at 0.2 A g^{-1} with active material loading around 4 mg cm^{-2}.

which is reduced to 185 Ω for Me-NQ. This suggests the facilitated reaction kinetics for Me-NQ. Galvanostatic intermittent titration technique (GITT) measurements are carried out to study the cation diffusion behaviors (Fig. 4b and c). The diffusion coefficient of NQ starts at the order of 10^{-10} cm^2 s^{-1} at the beginning of discharge, which decays and drops to the order of 10^{-12} cm^2 s^{-1} during the final stage of discharge. It evolves within the orders of 10^{-10} to 10^{-11} cm^2 s^{-1} during charge. For Me-NQ, the diffusion coefficients are mostly in the order of 10^{-10} cm^2 s^{-1} during both the discharge and charge processes. This confirms the faster cation diffusion in Me-NQ in comparison to NQ. Cyclic voltammetry (CV) tests are further carried out

to separate the charge storage processes (Fig. 4d and e). The non-diffusion and diffusion-controlled percentages are calculated according to the equation $i = k_1 v + k_2 v^{1/2}$ and the results are summarized in Fig. 4f. With the NQ cathode, the non-diffusion-controlled process contributes to 53% of overall capacity at 1.0 mV s^{-1}, which increases to 57%, 60%, 63%, 65% and 68% with the increase of scan rates to 1.2, 1.4, 1.6, 1.8 and 2.0 mV s^{-1}, respectively. In comparison, higher percentages of 66%, 69%, 71%, 73%, 74% and 76% are obtained with the Me-NQ cathode at the corresponding scan rates. The above results confirm the facilitated reaction kinetics of Me-NQ compared to NQ. Therefore, the Me-NQ cathode delivers higher practical
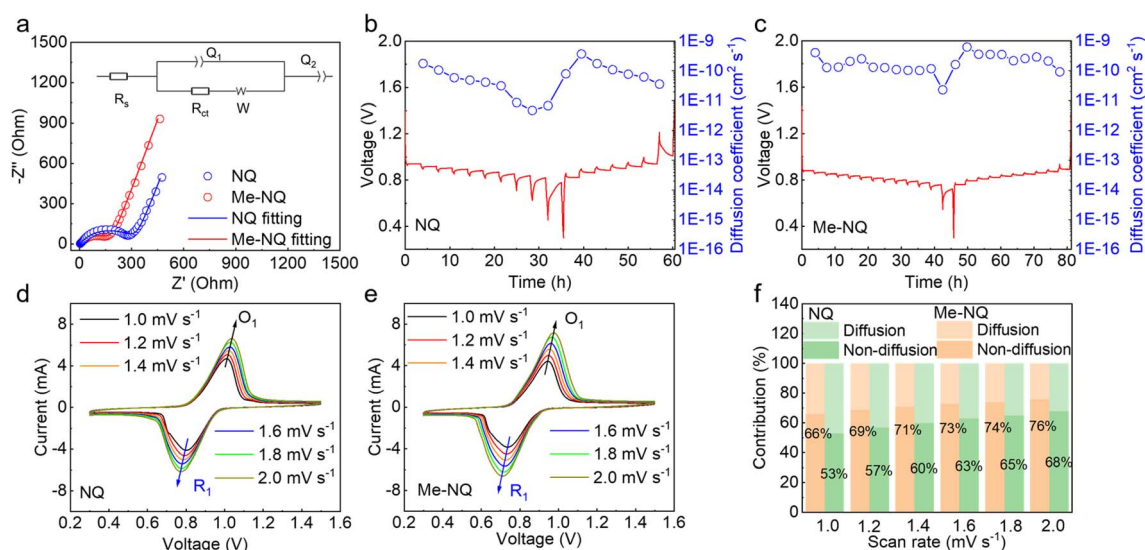

Fig. 4 (a) Nyquist plots and the corresponding fitted curves of NQ and Me-NQ. GITT curves and cation diffusion coefficients of (b) NQ and (c) Me-NQ. CV curves of (d) NQ and (e) Me-NQ cathodes at various scan rates, and (f) the calculated non-diffusion-controlled and diffusion-controlled contributions at various scan rates.

capacity at various current densities than NQ despite the slightly lower theoretical capacity of the former. Besides, the lower solubility and faster self-saturation process of Me-NQ also retain the majority of the active material at the cathode and ensure higher capacity.

The energy storage mechanism of the Me-NQ cathode in aqueous zinc cells is investigated. The redox active sites are studied by FT-IR. As shown in Fig. 5a, the characteristic peak of C=O at 1664 cm^{-1} disappears during discharge and appears upon charge (green region). Simultaneously, the peak at 1103 cm^{-1}, which is attributed to the C–O bond (pink region),[43,44] also shows reversible appearance and disappearance upon discharge and charge. This suggests the reduction of C=O on Me-NQ to C–O during discharge and reversible oxidation during subsequent charge. In accordance, the molecular electrostatic potential (ESP) map of Me-NQ in Fig. 5b shows the most negative regions at carbonyl groups, confirming them as the electrochemically active sites.

The cations stored in Me-NQ are studied by testing the cathodes in different electrolytes of ZnSO$_4$ with pH = 4, H$_2$SO$_4$ with pH = 1, and ZnSO$_4$ with pH adjusted to 1 using H$_2$SO$_4$. Fig. 5c compares the CV curves at 0.1 mV s^{-1}. Interestingly, the two ZnSO$_4$ electrolytes with different pH values show close peak positions. This suggests that the Zn^{2+} cation is favorable. Meanwhile, in the Zn^{2+} free H$_2$SO$_4$ electrolyte, a pair of redox peaks is observed at higher potential in comparison to the ones in zinc electrolytes. It demonstrates the proton storage

capability of Me-NQ. The peak shift is attributed to the Nernst shift as well as the different reaction potentials with Zn^{2+} and H$^+$ cations. Fig. 5d compares the XRD patterns of the cathode at different states. The Me-NQ active material exhibits poor crystallinity, and diffractions from KB, PTFE and filter paper adhered to the cathode are observed in the charged electrode. At the end of discharge, extra peaks attributing to Zn$_4$SO$_4$(OH)$_6 \cdot 3/4$H$_2$O show up. In the SEM image of the discharged electrode, flakes are found over the active material particles (Fig. 5e), which is the typical morphology of zinc basic salts. They disappear upon charge. Their formation/dissolution result from the pH decrease/increase in the cathode region,[35] which is further attributed to the reversible proton insertion/de-insertion in Me-NQ. Besides, the energy dispersive X-ray spectroscopy (EDS) mappings of the discharged cathode show the homogeneous distributions of C, O, S and Zn elements (Fig. 5f). The Zn signal results from zinc basic salts as well as Zn stored in the cathode. Density functional theory (DFT) calculations of Me-NQ binding with H$^+$ or Zn^{2+} provide further insights into the cation storage behavior. As summarized in Fig. 5g, the binding becomes stronger with more proton interactions in comparison to Zn^{2+}. This suggests an easier proton insertion in Me-NQ. Nevertheless, since the concentration of Zn^{2+} in the ZnSO$_4$ electrolyte is much higher than that of H$^+$, Zn^{2+} cations are also involved in the energy storage process. Overall, the above analysis confirms the co-storage of Zn^{2+} and H$^+$ on the carbonyl sites of the Me-NQ cathode with excellent reversibility in
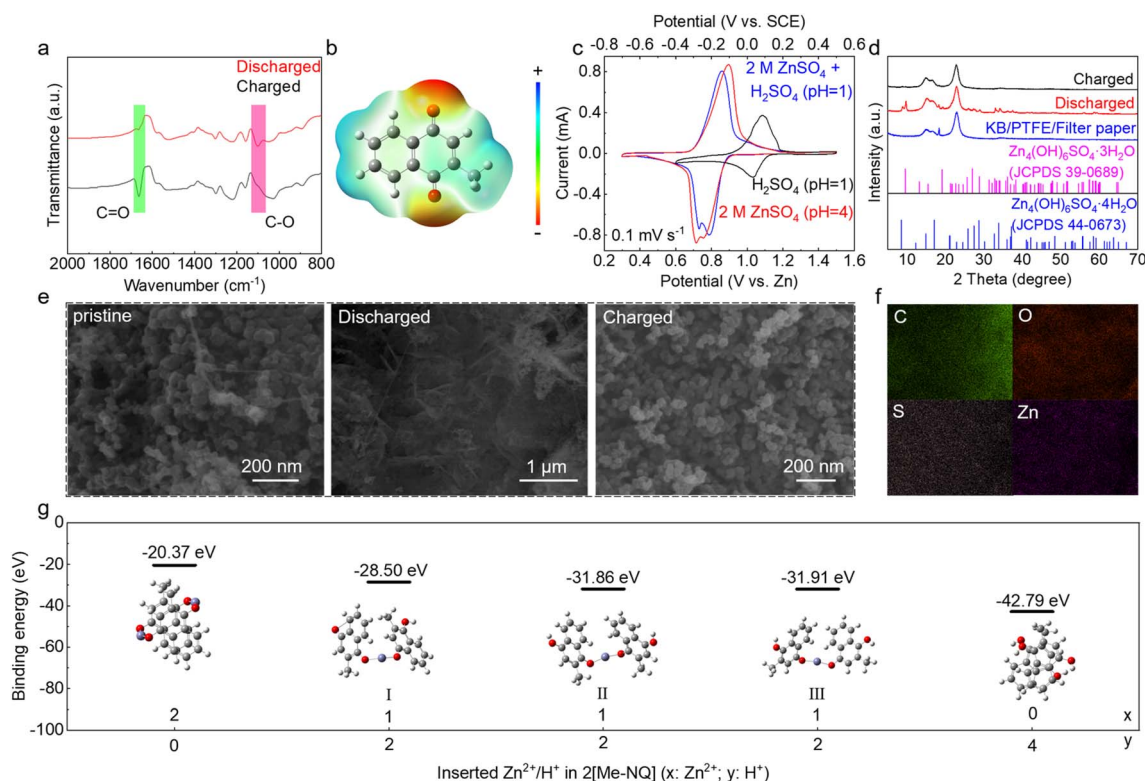

Fig. 5 (a) FT–IR of Me–NQ at different states. (b) ESP map of Me–NQ. (c) CV of Me–NQ in different electrolytes at 0.1 mV s^{-1}. (d) XRD patterns and (e) SEM images of Me–NQ at different states. (f) EDS mappings of the discharged Me–NQ. (g) Binding energies of two Me–NQ molecules with different numbers of Zn^{2+} and H$^+$.

aqueous zinc cells. Notably, characterization studies also reveal the reversible change of the carbonyl group and cation co-storage capability with the NQ cathode (Fig. S7†), demonstrating that the reaction mechanism is not affected with the introduction of the methyl group.

Conclusions

In this work, we present a facile self-saturation strategy for a small molecule menaquinone cathode material to realize stable cycling in aqueous zinc batteries. Considering the balance among cycling stability, capacity and voltage, a hydrophobic methyl group with light weight and a weak electron-donation effect is introduced on the parent NQ molecule. The solubility of the resulting Me-NQ reduces to only around one third that of NQ. This allows a facile self-saturation behavior in zinc cells of the former as confirmed by *in situ* UV-vis analysis, which inhibits continuous active material dissolution from the cathode and capacity decay. As a result, the Me-NQ cathode retains 236 mA h g^{-1} capacity after 100 cycles at 0.2 A g^{-1} and 146 mA h g^{-1} after 3500 cycles at 5 A g^{-1}, which are superior to 153 mA h g^{-1}/88 mA h g^{-1} of NQ under the same conditions. Me-NQ also presents faster reaction kinetics in comparison to NQ. Finally, the co-storage of Zn^{2+} and H^{+} on the carbonyl groups of Me-NQ is confirmed by combined experimental and theoretical analysis. Our work presents a general strategy to enhance the cycling stability of small molecule quinone cathode materials. It would also find applications for further molecular designs of electrode materials to solve dissolution issues.

Author contributions

S. L., G. Z. and X. S. conceived and designed this work. S. L. and G. Z. carried out all experimental measurements. G. Z. carried out all theoretical calculations. All authors participated in the analysis of the data and discussed and revised the manuscript.

Data availability

The data supporting this article have been included in the main text and the ESI.†

Conflicts of interest

There are no conflicts to declare.

Acknowledgements

References

1 N. Chang, Y. Yin, M. Yue, Z. Yuan, H. Zhang, Q. Lai and X. Li, A cost-effective mixed matrix polyethylene porous membrane for long-cycle high power density alkaline zinc-based flow batteries, *Adv. Funct. Mater.*, 2019, **29**, 1901674.

2 H. Chen, Z. Guo, H. Wang, W. Huang, F. Pan and Z. Wang, A liquid metal interlayer for boosted charge transfer and dendrite-free deposition toward high-performance Zn anodes, *Energy Storage Mater.*, 2023, **54**, 563–569.

3 S. Chen, M. Zhang, P. Zou, B. Sun and S. Tao, Historical development and novel concepts on electrolytes for aqueous rechargeable batteries, *Energy Environ. Sci.*, 2022, **15**, 1805–1839.

4 H. Li, M. Cao, Z. Fu, Q. Ma, L. Zhang, R. Wang, F. Liang, T. Zhou and C. Zhang, A covalent organic framework as a dual-active-center cathode for a high-performance aqueous zinc-ion battery, *Chem. Sci.*, 2024, **15**, 4341–4348.

5 M. Li, C. Liu, J. Meng, P. Hei, Y. Sai, W. Li, J. Wang, W. Cui, Y. Song and X.-X. Liu, Hydroxylated manganese oxide cathode for stable aqueous zinc-ion batteries, *Adv. Funct. Mater.*, 2024, DOI: 10.1002/adfm.202405659.

6 D. Ma, H. Zhao, F. Cao, H. Zhao, J. Li, L. Wang and K. Liu, A carbonyl-rich covalent organic framework as a high-performance cathode material for aqueous rechargeable zinc-ion batteries, *Chem. Sci.*, 2022, **13**, 2385–2390.

7 G. Ma, Z. Ju, X. Xu, Y. Xu, Y. Sun, Y. Wang, G. Zhang, M. Cai, L. Pan and G. Yu, Enhancing organic cathodes of aqueous zinc-ion batteries via utilizing steric hindrance and electron cloud equalization, *Chem. Sci.*, 2023, **14**, 12589–12597.

8 T. Sun, W. Zhang, Z. Zha, M. Cheng, D. Li and Z. Tao, Designing a solubility-limited small organic molecule for aqueous zinc-organic batteries, *Energy Storage Mater.*, 2023, **59**, 102778.

9 Y. Wang, C. Wang, Z. Ni, Y. Gu, B. Wang, Z. Guo, Z. Wang, D. Bin, J. Ma and Y. Wang, Binding zinc ions by carboxyl groups from adjacent molecules toward long-life aqueous zinc-organic batteries, *Adv. Mater.*, 2020, **32**, 2000338.

10 G. Zhang, J. Zhu, L. Lin, Y. Liu, S. Li, Q. Li, X.-X. Liu and X. Sun, A polydopamine coating enabling the stable cycling of MnO$_2$ cathode materials in aqueous zinc batteries, *Chem. Sci.*, 2024, **15**, 3545–3551.

11 D. Zhao, X. Pu, S. Tang, M. Ding, Y. Zeng, Y. Cao and Z. Chen, δ-VOPO$_4$ as a high-voltage cathode material for aqueous zinc-ion batteries, *Chem. Sci.*, 2023, **14**, 8206–8213.

12 S. Zheng, D. Shi, D. Yan, Q. Wang, T. Sun, T. Ma, L. Li, D. He, Z. Tao and J. Chen, Orthoquinone-based covalent organic frameworks with ordered channel structures for ultrahigh performance aqueous zinc-organic batteries, *Angew. Chem., Int. Ed.*, 2022, **61**, e202117511.

13 Q.-Q. Sun, J.-Y. Du, T. Sun, Z.-B. Zhuang, Z.-L. Xie, H.-M. Xie, G. Huang and X.-B. Zhang, Spatial structure design of thioether-linked naphthoquinone cathodes for high-

performance aqueous zinc-organic batteries, *Adv. Mater.*, 2024, **36**, 2313388.

14 T. Sun, Z. Yi, W. Zhang, Q. Nian, H. J. Fan and Z. Tao, Dynamic balance of partial charge for small organic compound in aqueous zinc-organic battery, *Adv. Funct. Mater.*, 2023, **33**, 2306675.

15 J. Wang, X. Zhang, Z. Liu, J. Yu, H.-G. Wang, X.-L. Wu, F. Cui and G. Zhu, Tuning electron delocalization of redox-active porous aromatic framework for low-temperature aqueous Zn-K hybrid batteries with air self-chargeability, *Angew. Chem., Int. Ed.*, 2024, **63**, e202401559.

16 W. Wang, Y. Tang, J. Liu, H. Li, R. Wang, L. Zhang, F. Liang, W. Bai, L. Zhang and C. Zhang, Boosting the zinc storage of a small-molecule organic cathode by a desalinization strategy, *Chem. Sci.*, 2023, **14**, 9033–9040.

17 L. Cheng, Q. Zhu, J. Liang, M. Tang, Y. Yang, S. Wang, P. Ji, G. Wang, W. Chen, X. Zhang and H. Wang, Flexible Electron-Rich Ion Channels Enable Ultra fast and Stable Aqueous Zinc-Ion Storage, *ACS Appl. Mater. Interfaces*, 2021, **13**, 54096–54105.

18 Y. Li, Y. Wang, Y. Xu, W. Tian, J. Wang, Li. Cheng, H. Yue, R. Ji, Q. Zhu, H. Yuan and H. Wang, Dynamic Biomolecular "Mask" Stabilizes Zn Anode, *Small*, 2022, **18**, 2202214.

19 M. Tang, Q. Zhu, P. Hu, L. Jiang, R. Liu, J. Wang, L. Cheng, X. Zhang, W. Chen and H. Wang, Ultrafast Rechargeable Aqueous Zinc-Ion Batteries Based on Stable Radical Chemistry, *Adv. Funct. Mater.*, 2021, **31**, 2102011.

20 W. Sun, F. Wang, S. Hou, C. Yang, X. Fan, Z. Ma, T. Gao, F. Han, R. Hu, M. Zhu and C. Wang, Zn/MnO$_2$ battery chemistry with H$^+$ and Zn^{2+} coinsertion, *J. Am. Chem. Soc.*, 2017, **139**, 9775.

21 Z. Shi, C. Zhou, F. Yang, L. Shan, B. Tang, J. Zhang, Q. Nan, Y. Xie, J. Li, H. Li and X. Tian, *ACS Energy Lett.*, 2024, **9**, 1063–1072.

22 J. Guan, Q. Huang, L. Shao, X. Shi, D. Zhao, L. Wang and Z. Sun, Polyanion-type Na$_3$V$_2$(PO$_4$)$_2$F$_3$@rGO with high-voltage and ultralong-life for aqueous zinc ion batteries, *Small*, 2023, **19**, 2207148.

23 J. Guo, W. Ma, Z. Sang, X. Zhang, J. Liang, F. Hou, W. Si, S. Wang and D. Yang, Low-cost, low-strain and lattice-water-rich Mn$_{0.25}$(VO)$_{0.75}$PO$_4$·2.25H$_2$O as high-rate and stable cathodes for aqueous Zn-ion batteries, *Chem. Eng. J.*, 2022, **428**, 132644.

24 Y. Sun, Z. Xu, X. Xu, Y. Nie, J. Tu, A. Zhou, J. Zhang, L. Qiu, F. Chen, J. Xie, T. Zhu and X. Zhao, Low-cost and long-life Zn/Prussian blue battery using a water-in-ethanol electrolyte with a normal salt concentration, *Energy Storage Mater.*, 2022, **48**, 192–204.

25 K. Wang, H. Li, G. Guo, L. Zheng, S. Passerini and H. Zhang, Enabling multi-electron reactions in NASICON positive electrodes for aqueous zinc-metal batteries, *ACS Energy Lett.*, 2023, **8**, 1671–1679.

26 G. Yang, Z. Liang, Q. Li, Y. Li, F. Tian and C. Wang, Epitaxial core-shell MnFe prussian blue cathode for highly stable aqueous zinc batteries, *ACS Energy Lett.*, 2023, **8**, 4085–4095.

27 Y. Zeng, X. Lu, S. Zhang, D. Luan, S. Li and X. Lou, Construction of Co-Mn prussian blue analog hollow spheres for efficient aqueous Zn-ion batteries, *Angew. Chem., Int. Ed.*, 2021, **60**, 22189–22194.

28 M. Chen, W. Zhu, H. Guo, Z. Tian, L. Zhang, J. Wang, T. Liu, F. Lai and J. Huang, Tightly confined iodine in surface-oxidized carbon matrix toward dual-mechanism zinc-iodine batteries, *Energy Storage Mater.*, 2023, **59**, 102760.

29 Y. Guo, R. Chua, Y. Chen, Y. Cai, E. J. J. Tang, J. J. N. Lim, T. H. Tran, V. Verma, M. W. Wong and M. Srinivasan, Hybrid electrolyte design for high-performance zinc-sulfur battery, *Small*, 2023, **19**, 2207133.

30 T. Liu, H. Wang, C. Lei, Y. Mao, H. Wang, X. He and X. Liang, Recognition of the catalytic activities of graphitic N for zinc-iodine batteries, *Energy Storage Mater.*, 2022, **53**, 544–551.

31 Y. Zhang, A. Amardeep, Z. Wu, L. Tao, J. Xu, D. J. Freschi and J. Liu, A tellurium-boosted high-areal-capacity zinc-sulfur battery, *Adv. Sci.*, 2024, **11**, 2308580.

32 D. Kundu, P. Oberholzer, C. Glaros, A. Bouzid, E. Tervoort, A. Pasquarello and M. Niederberger, Organic cathode for aqueous Zn-ion batteries: taming a unique phase evolution toward stable electrochemical cycling, *Chem. Mater.*, 2018, **30**, 3874–3881.

33 Z. Ye, S. Xie, Z. Cao, L. Wang, D. Xu, H. Zhang, J. Matz, P. Dong, H. Fang, J. Shen and M. Ye, High-rate aqueous zinc-organic battery achieved by lowering HOMO/LUMO of organic cathode, *Energy Storage Mater.*, 2021, **37**, 378–386.

34 Y. Wang, H. Cui, R. Li, C. Yue, H. Pan, Z. Tang, X. Wang, Y. Lin, H. Li, C. Han, D. Nan, C. Zhi and H. Lv, Bistate-type ion storage of azo polymer for aqueous zinc ion battery, *Energy Storage Mater.*, 2024, **65**, 103102.

35 J. Guo, J.-Y. Du, W.-Q. Liu, G. Huang and X.-B. Zhang, Revealing hydrogen bond effect in rechargeable aqueous zinc-organic batteries, *Angew. Chem., Int. Ed.*, 2024, **63**, e202406465.

36 Z. Lin, H.-Y. Shi, L. Lin, X. Yang, W. Wu and X. Sun, A high capacity small molecule quinone cathode for rechargeable aqueous zinc-organic batteries, *Nat. Commun.*, 2021, **12**, 4424.

37 C. Li, L. Hu, X. Ren, L. Lin, C. Zhan, Q. Weng, X. Sun and X. Yu, Asymmetric charge distribution of active centers in small molecule quinone cathode boosts high-energy and high-rate aqueous zinc-organic batteries, *Adv. Funct. Mater.*, 2024, **34**, 2313241.

38 S. Li, J. Shang, M. Li, M. Xu, F. Zeng, H. Yin, Y. Tang, C. Han and H.-M. Cheng, Design and synthesis of a π-conjugated N-heteroaromatic material for aqueous zinc-organic batteries with ultrahigh rate and extremely long life, *Adv. Mater.*, 2023, **35**, 2207115.

39 W. Wang, S. Zhang, L. Zhang, R. Wang, Q. Ma, H. Li, J. Hao, T. Zhou, J. Mao and C. Zhang, Electropolymerized bipolar Poly(2,3-diaminophenazine) cathode for high-performance aqueous Al-ion batteries with an extended temperature range of -20 to 45 °C, *Adv. Mater.*, 2024, **36**, 2400642.

40 M. Xue, J. Bai, M. Wu, Q. He, Q. Zhang and L. Chen, Carbon-assisted anodes and cathodes for zinc ion batteries: From

basic science to specific applications, opportunities and challenges, *Energy Storage Mater.*, 2023, **62**, 102940.

41 T. Yokoji, H. Matsubara and M. Satoh, Rechargeable organic lithium-ion batteries using electron-deficient benzoquinones as positive-electrode materials with high discharge voltages, *J. Mater. Chem. A*, 2014, **2**, 19347–19354.

42 Z. Xu, M. Li, W. Sun, T. Tang, J. Lu and X. Wang, An ultrafast, durable, and high-loading polymer anode for aqueous zinc-ion batteries and supercapacitors, *Adv. Mater.*, 2022, **34**, 2200077.

43 Z. Lin, L. Lin, J. Zhu, W. Wu, X. Yang and X. Sun, An anti-aromatic covalent organic framework cathode with dual-redox centers for rechargeable aqueous zinc batteries, *ACS Appl. Mater. Interfaces*, 2022, **14**, 38689–38695.

44 J. Yang, Z. Wang, Y. Shi, P. Sun and Y. Xu, Poorly soluble 2,6-Dimethoxy-9,10-anthraquinone cathode for lithium-ion batteries: the role of electrolyte concentration, *ACS Appl. Mater. Interfaces*, 2020, **12**, 7179–7185.